PHOTONICS Research

Buildup dynamics of multiple solitons in spatiotemporal mode-locked fiber lasers

Kewei Liu,[1] Xiaosheng Xiao,[2,4] Yihang Ding,[1] Hongyan Peng,[3] Dongdong Lv,[3] and Changxi Yang[1,5]

[1]State Key Laboratory of Precision Measurement Technology and Instruments, Department of Precision Instruments, Tsinghua University, Beijing 100084, China
[2]State Key Laboratory of Information Photonics and Optical Communications, School of Electronic Engineering, Beijing University of Posts and Telecommunications, Beijing 100876, China
[3]School of Physics and Electronic Engineering, Hainan Normal University, Haikou 571158, China
[4]e-mail: xsxiao@bupt.edu.cn
[5]e-mail: cxyang@tsinghua.edu.cn

Received 22 April 2021; revised 31 July 2021; accepted 3 August 2021; posted 3 August 2021 (Doc. ID 428687); published 8 September 2021

Spatiotemporal mode locking is a nonlinear process of multimode soliton self-organization. Here the real-time buildup dynamics of the multiple solitons in a spatiotemporal mode-locked multimode fiber laser are investigated, assisted by the time-stretch technique. We find that the buildup processes are transverse mode dependent, especially during the stages of relaxation oscillation and *Q*-switching prior to multiple soliton formation. Furthermore, we observe that the transverse modal composition of these generated pulses among the multiple solitons can be different from each other, indicating the spatiotemporal structure of the multiple soliton. A simplified theoretical model based on pulse energy evolution is put forward to interpret the role of 3D saturable absorber on spatiotemporal structures of spatiotemporal mode-locking multiple solitons. Our work has presented the spatiotemporal nonlinear dynamics in multimode fiber lasers, which are novel to those inside the single transverse mode fiber lasers.

https://doi.org/10.1364/PRJ.428687

1. INTRODUCTION

The multiple soliton in mode-locked lasers is a widely observed phenomenon that has been extensively investigated over the years [1–5]. Assisted by the ultrafast single-shot measurement dispersive Fourier transform (DFT, or time stretch) [6,7], a plethora of transient dynamics of different kinds of multiple solitons, including soliton molecules and harmonic mode locking have been revealed in detail. For example, the internal interactions [8–10] and buildup dynamics [11,12] of soliton molecules, the birth and collision of multiple solitons [13], the entire birth of harmonic mode locking [14,15] and multiple solitons [16], as well as the transition between different multipulsing states [17], were characterized in real time, having provided much insight on comprehending the complexities of dissipative solitons. These investigations are based on mode-locked lasers with a single transverse mode, which have been the mainstream area of scientific exploration and applications in recent decades.

Remarkably, the demonstration of spatiotemporal mode locking (STML) in multimode fiber lasers, where both the longitudinal and transverse modes are simultaneously locked in cavity, has opened up a new frontier, enabling investigations on multidimensional nonlinear problems that are related to quantities of real-world physical phenomena [18]. Massive progress has been achieved during the years in implementing novel configurations and exploring the nonlinear dynamics of three-dimensional (3D) solitons generated in STML lasers, which have expanded the concepts on their one-dimensional (1D) counterparts. A few of these include soliton molecules [19], multiple solitons [20], breathers and optical vortices [21], wavelength-switchable pulses and hysteresis [22], self-similar solitons [23], beam self-cleaning [24], transition between *Q* switching and STML [25], and period-doubling bifurcation [26]. In addition, it has been manifested in our recent work that STML can also be achieved in multimode fiber lasers with commercially available multimode fibers that possess large modal dispersion [27], which advances the development of useful STML lasers accessible for applications. Besides the experimental efforts, a theoretical model, attractor dissection, was proposed to comprehensively understand the mechanisms of STML [28]. There is great significance in studying 3D optical analogs, which are overwhelmingly connected to important problems in the field of nonlinear science, while the ability to efficiently probe the dynamics of the formation, evolution, and interaction of 3D dissipative solitons is highly demanding. Nevertheless, the exploration of the transient dynamics of 3D dissipative solitons in STML lasers, though having attracted broad interest, is still in its infancy. Very recently, the transient

and random phenomena of multimode solitons have been characterized by spatiotemporal spectral imaging [29]. In addition, various dynamics in an STML laser have been observed by means of real-time multispeckle measurement [30], shedding much light on comprehending the multidimensional physical nature of 3D solitons.

In this work, we investigate the buildup dynamics of multiple-soliton states in an STML laser. Taking advantage of the dual-channel DFT measurement, where two spatial sampling channels simultaneously track the real-time data containing two different transverse mode components, we discovered plenty of curious phenomena during the generations of multiple STML solitons without analogs in their 1D counterparts. There exhibit pronounced distinctions between the evolving dynamics in two channels, especially from the early stages to the establishment of the multiple solitons. In addition, we find the existence of multiple STML solitons with nonequivalent peak intensities. There, different pulses can possess diverse transverse mode components, which is quite different from our previous demonstration of multiple solitons in STML lasers [20]. The results can not only extend the scope of multiple solitons in 1D platforms, but also accelerate the understanding of high-dimensional nonlinear physics.

2. EXPERIMENTAL SETUP

The overall schematic of the multimode cavity and measurement system is shown in Fig. 1. A 980 nm multimode laser diode pump launches, via a collimating lens L_1, into a 0.55 m long step index gain fiber (Nufern LMA-YDF-20/125-9M, NA = 0.08, supporting up to six transverse modes). The gain fiber is spliced to a segment of 5.35 m graded-index (GRIN) multimode fiber (YOFC-OM4, with core/cladding diameter of 50/125 μm). The laser loop is completed with a mirror (M) and a short-pass dichroic mirror (SPDM) that couples spatial light back to the gain fiber. This coupling naturally serves as a spatial filter needed for STML [18], as it allows only part of the spatial components of light to couple back to the gain fiber. Nonlinear polarization rotation (NPR) is introduced, which is responsible for the mode-locking operation. We note the laser configuration is similar to our previous scheme [25,27]. However, as the cavity has quantities of degrees of freedom, especially in cavity spatial coupling, the laser can present different nonlinear dynamics even with the similar cavity structure. The multimode laser is extracted by a polarized beam splitter (PBS) and then split by two beam splitters (BSs), and is intended for beam profile visualization (using a near-IR camera) and subsequent spatial sampling [18,20]. As illustrated in Fig. 1, the output beam is collected by two spatial samplers, which are two collimators integrated with single-mode fibers in our scheme. This sampling method constitutes a simple but effective space-resolved measurement, since the two sampling channels extract different spatial parts of the output beam, which contains two different spatial-mode components. The two multimode-to-single-mode conversions in this sampling process will reflect the dynamics of different transverse-mode components. Each branch of light is amplified by an ytterbium-doped fiber amplifier (YDFA) before entering the optical delay line (ODL) for pulse stretching. Both delay lines are composed of single-mode fiber with nearly equivalent total length (12.5 km) to ensure equal propagating time of the two channels of light. The signals are simultaneously received by photodetectors (PDs), then digitalized and displayed by a multichannel oscilloscope (Keysight Infiniium DSOS804A, bandwidth, 8 GHz; sampling rate, 20 GSa/s). The length differences of the two ODLs are calibrated by recording the time points when the CW light vanishes in each channel after blocking the laser cavity, in the case when the two sampling branches sample from the same spatial position of the beam. The recorded data are finally processed, ready for the reconstruction of the buildup process of mode-locked pulses.

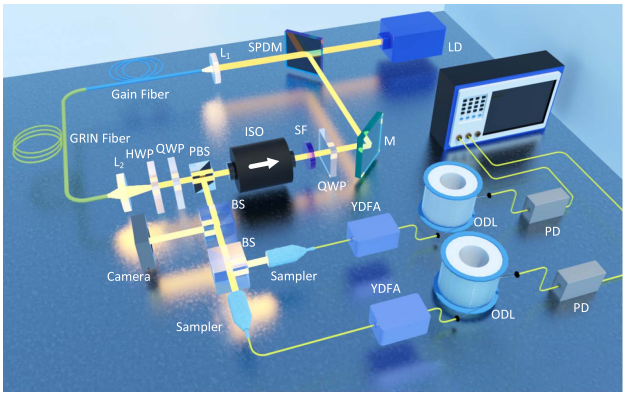

Fig. 1. Experimental setup of the STML fiber laser and system of DFT for real-time measurement. LD, laser diode; SPDM, short-pass dichroic mirror; L_1, L_2, lens; M, mirror; ISO, isolator; SF, spectral filter; HWP, half-wave plate; QWP, quarter-wave plate; PBS, polarization beam splitter; BS, beam splitter; YDFA, ytterbium-doped fiber amplifier; ODL, optical delay line; PD, photodetector.

In our experiments, the threshold pump power for single-pulse STML operation is 4.5 W. After tuning up the pump to 6.5 W, various steady multiple solitons, including soliton bunches and high-order harmonic mode locking, can be achieved (see Appendix A). The validation of STML can be found in Appendix B. The number of pulses in the STML state varies with the NPR states (by adjusting the rotation angles of three wave plates). In addition, the number of generated pulses as well as their relative distances and intensities is stochastic with each buildup process, even at a fixed pump power level (see Appendix A). The uncertainty of a generated pulse number with fixed pump power does not conform to the energy-quantization law [3,31] that applies in single transverse-mode platforms.

3. BUILDUP DYNAMICS OF MULTIPULSING STML

To gain insights into the buildup dynamics of spatiotemporal mode-locked multiple solitons, the real-time characterization utilizing the DFT method is implemented. As previously illustrated, two channels of spatial sampled light are launched into the ODLs for pulse stretching, and thus are mapped to the spectral profiles of the mode-locked pulses. In our experiment, the duration of the stretched pulses is around 5 ns, and the spectral resolution of the DFT is estimated to be 0.26 nm [7]. We first obtain a stable multiple pulsing regime at 6.5 W pump power. Then the laser is blocked by a chopper placed in

the cavity. As the chopper suddenly is removed, the oscilloscope is triggered and begins to record the data. Figure 2 shows a three-pulse STML buildup process. Two simultaneously sampled data in channels I and II are displayed in Fig. 2(a). The figures on the right panel of Fig. 2(a) are the extracted waveforms at around 2500 μs (denoted by the dashed lines) within one cavity round-trip time (i.e., 31.1 ns). The inset shows the corresponding beam profile (after mode locking), and the approximate sampling positions of the two channels are indicated by red circles and white arrows. It is easy to notice that the spectra of channels I and II are different, which further verifies the diverse spatial mode components of the two sampling branches.

We select the same portion of the recorded waveform data from channels I and II [see the dashed rectangle in Fig. 2(a)], slice them by cavity round-trip time, and then plot the 2D contour map exhibiting the real-time buildup over 58,000 round trips, shown in Fig. 2(b). The corresponding integrated energy evolution is displayed in Fig. 2(c). The single-shot spectral profile exhibits complex landscapes. According to the characteristics of pulse evolution, the overall buildup process can be divided into five phases, (i)-(v), denoted at the top of Figs. 2(b) and 2(c). In phase (i), fluctuations in background intensity along with multiple small peaks emerge as a typical sign of relaxation oscillation (RO). It is noticeable that the RO intensity in channel I in this phase is far lower than that in channel II. This might be a consequence of the rapidly changing beam profile because little light is collected at the spatial position of sampling channel I. During phase (ii), the Q-switching operation is achieved. The periodicity of Q-switched pulses is closely related to the energy level transitions, and it is slightly influenced by NPR states and pump power. The interval of Q-switched pulses (around 13.2 μs, corresponding to the repetition rate of 75.7 kHz). Despite unequal intensities of the giant pulses [also inferred from the energy evolution in Fig. 2(c)], the time interval of Q-switched pulses is equal, which is a major distinction from RO [32]. Pulses in phase (iii) exhibit the features of RO again. It can be clearly seen that multiple small pulses, carried by the energy fluctuating wave, pop up, split, and drift along the time axis, similar to the behaviors in phase (i). Note that the pulse drifting speeds between two channels are different, which is more pronounced in some buildup cases (see Appendix C, Fig. 9). The laser evolves to Q switching again in phase (iv).

Finally, multiple pulses rise up simultaneously in both channels in phase (v). This indicates that the transverse modes are almost mode-locked simultaneously. The zoom-in figures on the right panel in Fig. 2(b) display the detailed establishment

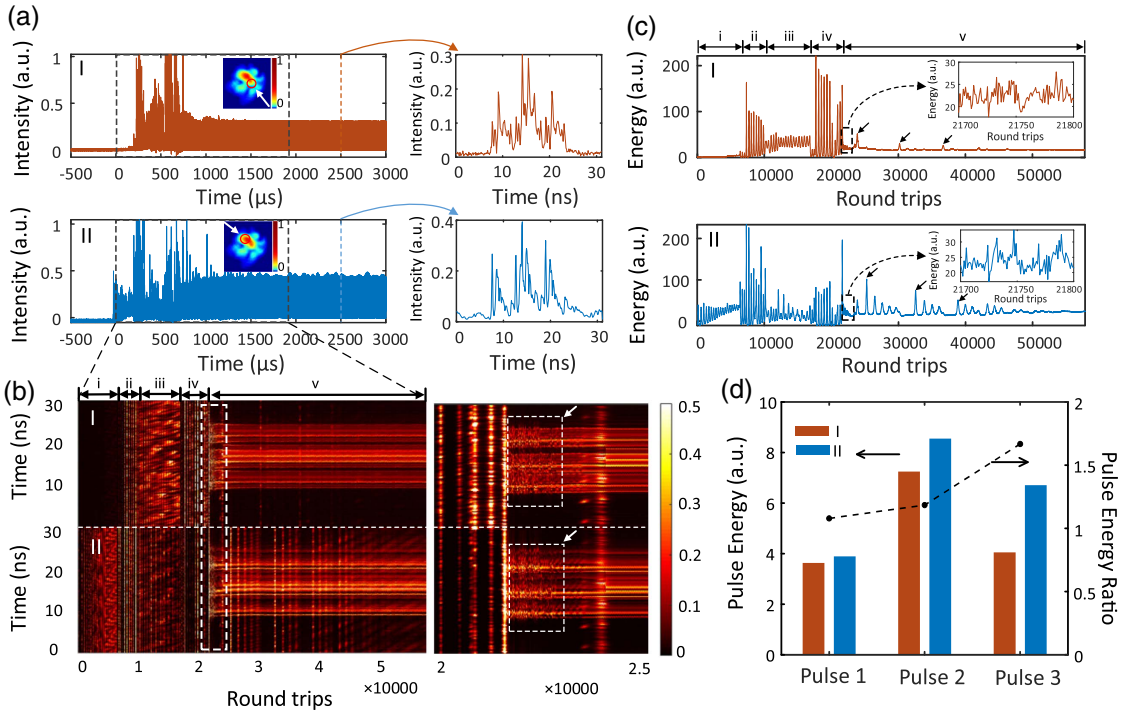

Fig. 2. Buildup dynamics of a three-pulse STML. (a) Experimental recordings of the multipulse buildup of two channels, I (orange) and II (blue), which are simultaneously acquired via two spatial sampling points. The two figures in the right panel exhibit the stretched pulse profiles at approximately 2500 μs within one cavity round-trip time (~31.1 ns), indicating diverse spectral profiles between two different channels. The inset shows the corresponding beam profile after steady mode locking, where the sampling positions of channels I and II are indicated by the red circles and white arrows. (b) Contour plot of the extracted experimental data ranging over 58,000 round trips. The figure in the right panel displays the close-up evolution (indicated by the white dashed rectangle in the figure on the left) near the establishment of mode-locked pulses. (c) Corresponding total energy evolution integrated within each round trip. The insets exhibit the zoom-in energy variation during the turbulent period [indicated by the white dashed rectangle and arrow on the right panel of (b)] of the buildup process. (d) Integrated energy of each stretched pulse (pulse 1, pulse 2, and pulse 3) of channels I and II after entering the stable STML state. The line graph shows the energy ratio of each stretched pulse between two different channels.

of the multiple pulses. At the very early stage in phase (v), the spectra in both channels exhibit turbulent oscillation, where both the intensities and widths of the spectra vary randomly upon pulse propagation, denoted by the white arrows and dashed rectangles. However, the evolving patterns of this random turbulence are different between the two channels. The distinctions are also indicated by the energy variation [see insets in Fig. 2(c), from the 21,700th to 21,800th round trip]. There, the overall energy in the two channels is not changing in pace with each other along the round-trip axis. There is a large possibility that modal competitions result in energy flowing from one transverse mode to another at the initial stages of final mode locking. In addition, it is noticeable that a series of damping spikes, with longer round-trip intervals, appear shortly after the establishment of the multipulses. The damping spikes are more prominent in channel II. In addition, the time when the most intensive RO fluctuation [marked by black arrows in Fig. 2(c)] appears is not the same for the two channels. These decaying spikes eventually perish, and stable multiple-pulse mode locking (without RO fluctuations) is achieved.

It is clear that among the steady multiple pulses, pulse 1, pulse 2, and pulse 3, have different pulse energy, with pulse 2 (in the middle) the highest. Their individual pulse energy (or spectral energy) after steady mode locking is displayed in Fig. 2(d). The black line represents the pulse energy ratio between the two channels. Since the spectral energy of different excited transverse modes is generally different, this ratio distinction intuitively implies the mode structures (i.e., the transverse-mode components) are diverse among the pulses, which is unique to multimode platforms. However, as for the cases where the pulses have identical energy, no such mode structures are exhibited; in other words, the mode component for each pulse is identical as well, which is coincident with our previous findings in Ref. [20]. Limited by the spatial sampling resolution, the light coupled into the two channels inevitably possesses common transverse mode components. Therefore, the mode distinctions between pulses that are indicated in Fig. 2(d) are underestimated.

Noteworthy is that each buildup process of the multiple solitons tends to be different, even with the same cavity configuration and pump power due to the stochastic multidimensional initial noises, which largely differ from the buildup cases in single-transverse mode platforms. In addition, factors such as spatial mode coupling, and the NPR initial states can influence the buildup process as well. At lower pump power levels, the single soliton is more likely to be generated. We note that the buildup process of one single soliton exhibits few substantial differences compared with the selected one single pulse in the multiple-soliton regimes, which possess weak pulse interactions in our laser.

In addition to the multiple-soliton buildup case shown in Fig. 2, we discovered some other interesting dynamics, such as asynchronous establishment of multiple pulses, pulse extinction, and pulsations (see Appendix C. Also see Visualization 1 for the animation of the buildup process of a four-soliton STML). Moreover, we observed STML with even more pulses, also termed as "soliton bunch." Soliton bunches exhibit themselves as a group of tight packets that usually possess unequal

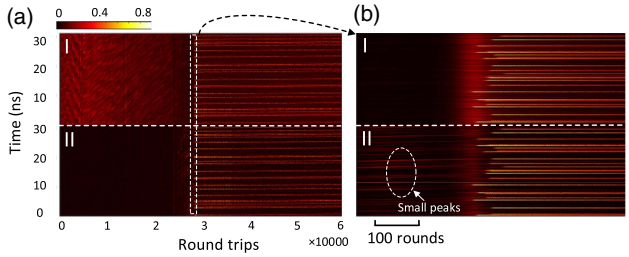

Fig. 3. Buildup dynamics of STML soliton bunch composed of 23 pulses. To avoid overlap, the pulses are not stretched. (a) Contour plot of the buildup process covering 60,000 round trips; (b) close-up of the soliton bunch generation, indicated by the white dashed rectangle in (a). There appear multiple small peaks that seed mode-locked pulses afterwards in channel II. While in channel I, these tiny peaks are barely observed. Note the buildup of different pulses is asynchronous. The maximum buildup time difference is around 50 round trips.

internal distances of phase differences between the pulses; they have been reported in single-mode fiber lasers [5,33]. To avoid overlap of soliton bunches, the pulses are not time-stretched by DFT in this case. Figure 3 shows the buildup of a soliton bunch containing 23 solitons. Similarly, there exhibits prominent distinction between two channels during RO. Besides, it can be clearly seen in Fig. 3(a) that multiple small pulses drift along the time axis as they are propagating in the cavity (along the round-trip axis) while their drifting speeds are time-varying, which is attributed to the change of group velocity of the small pulses. Previous to the final establishment of the soliton bunch, quantities of seeding peaks appear, which are clearly observed in channel II (denoted by the white circle). Following a moderate background fluctuation, bunches of solitons finally arise. From the zoom-in plot Fig. 3(b), the solitons are not simultaneously generated, but the differences of buildup time among pulses are not pronounced, with the maximum of merely around 50 round trips (~155 ns).

We would like to point out that due to the deficiency of the limited spatial resolution of the sampling method, the buildup dynamics shown in the two channels might lose some subtle details concerning the impact of modal interactions on the soliton evolutions. Further endeavors are necessary to give sufficient evidence to reveal the complete landscapes of the complex buildup dynamics of solitons in STML lasers.

4. THEORETICAL MODEL AND RESULTS

So far, the real-time characterization of the spatiotemporal evolutions of the soliton buildup process has revealed the multimode properties of multipulsing STML. It is anticipated that diverse dynamics are exhibited between different channels, which has manifested itself in the high-dimensional properties of STML lasers, especially in terms of the spatial dimension. Moreover, we have discovered, in the multipulsing STML regimes that possess unequal pulse energies, the transverse mode structures can vary from pulse to pulse. We currently speculate that the 3D saturable absorber plays a vital role in this phenomenon, inspired by our previous investigation on STML [27]. There, we have performed numerical simulations based on the generalized multimode nonlinear Schrödinger equation

(GMMNLSE), in which we discovered that the saturable absorber (SA) acts on the spatiotemporal intensity and possesses different effects on different transverse modes. To verify this assumption and further illustrate the observed spatiotemporal structure of steady multiple solitons, we adopt a simple theoretical model that takes an iterative form to solve the steady pulse energy. This quick convergent method has already been used in single-transverse mode-locked lasers [34,35]. Here we further adapt this model to multimode multiple solitons. The schematic of the model is displayed in Fig. 4(a). To identify the impact of the 3D SA, the interactions among different transverse modes (e.g., competitions and nonlinear coupling) in the gain media are neglected. But the gain competitions among the multiple solitons are still accounted for in order to get pulses with different energies. The amplified solitons undergo mode decomposition before passing through the SA. The SA is transverse-mode resolved. As for different modes, the modulation depths and the phase biases of the SA are different. The solitons are then mode-composited and returned to the gain media, completing a cycle of the iterative model. A detailed description of this mode can be found in Appendix D.

As a simple example, we consider a three-pulse STML containing three transverse modes. The simulation parameters can be found in Appendix D. The calculated normalized energy of each pulse in three different transverse modes (mode 1, mode 2, mode 3) versus pump power (equivalent to the gain saturable energy E_{sat}) is displayed in Fig. 4(b). As shown in Fig. 4(b), the solitons subsequently rise up upon the increase of E_{sat}. The E_{sat} thresholds of their establishment, namely, TH_1, TH_2, and TH_3, are approximately 1.0, 1.7, and 2.6, respectively. When E_{sat} is larger than TH_3, a three-pulse mode locking

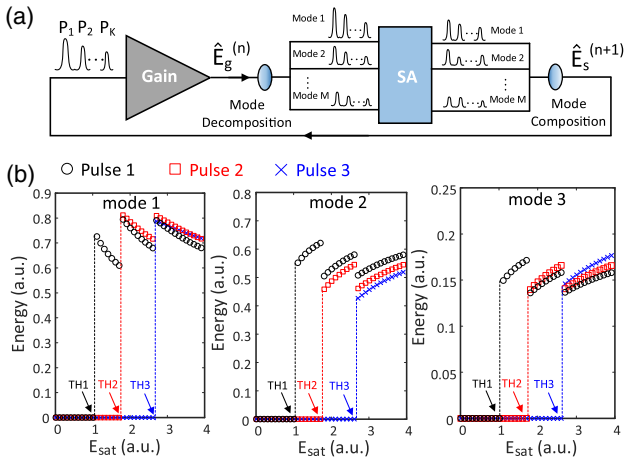

Fig. 4. Basic model and typical result of multiple-soliton generation. (a) Schematic of the iterative model to simulate multipulsing STML. The interactions among transverse modes in the gain media are neglected; thus the modes are amplified as a whole in the gain media. The SA is mode-dependent and transverse mode decomposition and composition are implemented before and after the SA, respectively. (b) Calculated energy of the pulses (pulse 1, pulse 2, pulse 3) for different transverse modes (mode 1, mode 2, and mode 3) versus the saturable energy E_{sat} (E_{sat} is closely related to the pump power). TH_1, TH_2, and TH_3 are the thresholds of pulse 1, pulse 2, and pulse 3, respectively.

with unequal pulse energies is supported. It is clear that the tendencies of pulse energy growth versus E_{sat} vary among the modes. All the pulse energies in mode 1 go down, while those in modes 2 and 3 ramp up with increasing E_{sat}. It is noteworthy that the energy relationships of the pulses are different for different transverse modes in this case. For example, in a three-soliton regime ($E_{sat} > 2.6$), the pulse with the highest energy in mode 2 is pulse 1 (black circle) but pulse 3 (blue cross) possesses the highest energy in mode 3. In other words, the pulse energy ratio varies from mode to mode. From another point of view, different pulses in this multipulsing STML regime have diverse transverse mode profiles, given that the energies of the excited modes are generally different, which echoes the experimental results to a certain degree.

5. DISCUSSION AND CONCLUSION

The simple theoretical model, considering the mode-dependent SA and gain competition among pulses, has thrown some light on comprehending the spatiotemporal structures of multiple solitons in STML lasers. It highlights the role of transverse mode-dependent nonlinear SA effects in forming the spatiotemporal structures of the pulses. When multiple solitons appear with unequal energies, the mode-dependent 3D SA results in the diverse mode component for different pulses. However, in a more rigorous sense, not only the 3D SA effects, but all the intermodal interactions, including modal competitions in the gain fiber and modal evolutions during nonlinear propagation, can contribute to the diverse mode components. Consider all the effects will make the model too complicated. Besides, we note that this simplified model only provides insights limited to the spatiotemporal structures of the solitons and is not capable of interpreting the observed complex evolution dynamics in our experiments. We note nonlinear intermodal coupling in the SA, which we neglect in our simple model, can also contribute to the complex buildup dynamics of solitons in the STML laser. More comprehensive and convincing results concerning the buildup dynamics as well as the spatiotemporal structures of STML solitons will be produced by performing numerical simulations based on a $(3+1)$-D generalized nonlinear Schrödinger equation (GNLSE), as well as a 3D SA model, in our future works. In addition, the interpretation of nonlinear interactions between different modes during the RO and Q-switching phases before eventual mode locking are also expected.

In conclusion, we observed various kinds of multiple solitons in an STML fiber laser, which broadens the concepts of 1D soliton counterparts. The buildup dynamics of STML multipulsing have been visualized by taking advantage of the DFT technology with multiple spatial sampling channels, where pronounced spatiotemporal distinctions exist among different transverse modes from the early stages to the soliton establishments. Specifically, the evolution patterns during the RO as well as Q-switching states vary for different transverse modes. In addition, we have discovered some particular multiple solitons regimes where the energies of the pulses are unequal. In these cases, the transverse mode structures can vary from pulse to pulse. We present a simplified theoretical model to illustrate the role of the mode-dependent 3D SA in forming

the spatiotemporal structures of the multiple solitons. The transverse-mode-dependent evolution pattern during the buildup process of solitons, as well as the discovered distinct mode components among the pulses, is unique to STML lasers, which lack analogs in traditional single transverse-mode platforms.

The 3D solitons in the multipulsing STML regimes manifest various complicated dynamics and unique spatiotemporal structures. Our demonstration has not only extended the scope of the currently limited discovery of STML lasers, but also shed some light on multidisciplinary nonlinear dynamics and contributed to understanding the complex physical nature of higher-dimensional problems.

APPENDIX A: VARIOUS KINDS OF MULTIPLE-SOLITON REGIMES IN THE STML LASER

In our experiment, various kinds of multipulsing regimes, including soliton bunches and harmonic mode locking, have been achieved, generally by tuning the rotation angles of the wave plates and altering the pump power. Figure 5 shows some typical pulse waveforms with 7.0 W pump power in different NPR states, including a second-harmonic mode locking [Fig. 5(a)], multiple solitons with equal pulse intensity [Fig. 5(b)], multiple solitons with unequal pulse intensities [Figs. 5(c) and 5(d)], as well as soliton bunches [displayed in Figs. 5(e) and 5(f)].

Particularly, we observed a high-order harmonic mode-locking state in the multimode laser. The temporal waveform and RF spectrum are, respectively, shown in Fig. 6(a) (inset: the beam profile) and Fig. 6(b). The frequency of the first highest peak (black arrow) in the RF spectrum, at around 834 MHz, is 26 times the fundamental frequency 32.1 MHz, wherein the highest sideband peak is around 25.9 dB lower than the main peak.

In a shorter cavity in our experiment, multiple pulses can still be achieved. The reduction of the cavity length is implemented by shortening the length of the passive multimode fiber (YOFC-OM4) from 5.35 m to 2.75 m. The spatial part of the cavity and the step index gain fiber remain unchanged. Figures 6(c) and 6(d) exhibit the waveform and spectrum, respectively, of a two-pulse STML. The beam profile is displayed in the inset of Fig. 6(d). The cavity FSR is approximately 56 MHz, corresponding to the round-trip time of 17.85 ns.

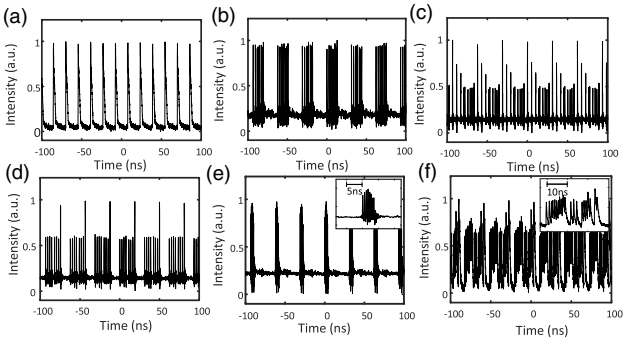

Fig. 5. Various multipulsing STML regimes containing different numbers of solitons. (a) Second-harmonic mode locking; (b) eight-soliton STML with equal pulse intensity; (c), (d) multiple-soliton STML with unequal pulse intensities; (e), (f) soliton bunches. The insets are the close-up of the pulses within one cavity FSR (~31.1 ns).

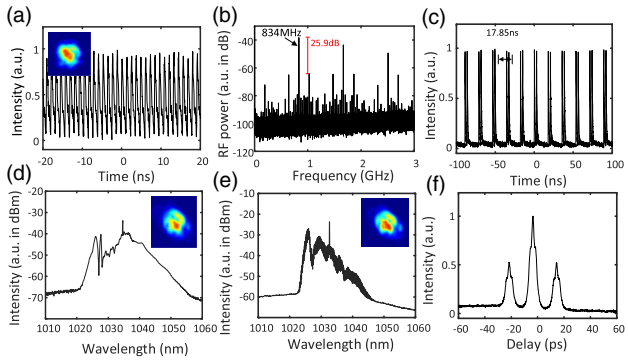

Fig. 6. (a)–(b) 26th-order harmonic STML state. The waveform is displayed in (a) with the inset showing the beam pattern. The first highest peak of (b) the RF spectrum is at approximately 834 MHz (26 times of the cavity FSR), possessing around 25.9 dB prominence to the highest side peak. (c), (d) two-soliton STML. The temporal waveform and spectrum are shown in (c) and (d), respectively. (e), (f) Soliton-molecule STML: (e) spectrum (inset is the beam profile); (f) autocorrelation trace.

A soliton molecule state is also achieved in the cavity [see the spectrum and beam profile in Fig. 6(e) and the inset, and autocorrelation trace in Fig. 6(f)].

APPENDIX B: VALIDATION OF THE STML

Generally, the spatial sampling and spectral filtering methods are utilized to validate the STML states [18,20]. Figure 7(a) is the RF spectrum of one multipulsing STML state. Figure 7(b) shows the spectra collected from three different beam spatial positions A, B, and C (denoted in the inset). The spatial-sampled spectra indicate that different transverse modes have diverse spectra, which is evidence of the multimode operation of the STML laser [18–20,25,26]. Figure 7(c) displays the filtered spectra and beam profiles after spectral filtering. The entire and the filtered spectra via a short-pass filter (filter 1) and a long-pass filter (filter 2) along with the corresponding beam profiles (in the right column) further prove the multimode properties of the multipulsing STML state. Note that spatial sampling and spectral filtering are not conducted in the same STML state, so the spectra in Figs. 7(b) and 7(c) are not identical, which, however, does not interfere with the confirmation of STML.

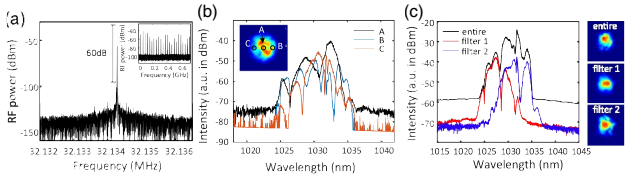

Fig. 7. Validation of STML of the multiple solitons in the multimode fiber laser cavity. (a) RF spectrum (inset, wide-range RF signal); (b) spectra extracted from three spatial positions A, B, C, denoted in the beam profile (the inset); (c) spectra of the entire output and the spectral-filtered outputs after the short-pass filter (filter 1) and long-pass filter (filter 2) with the corresponding beam profiles in the right column.

APPENDIX C: TWO OTHER BUILDUP PROCESSES OF THE MULTIPULSING STML

Since the STML laser is seeded by random multidimensional noises (or perturbations), the multiple-soliton buildup evolution pattern is stochastic from case to case. In this section, we show another two representative buildup processes, still with 6.5 W pump power, of the multipulsing STML that exhibits distinct evolving dynamics. Figure 8 exhibits the buildup dynamics of a four-soliton STML. The recorded experimental data sampled from two channels are shown in Fig. 8(a). The figures in the right column are the close-up waveforms within one cavity round trip (~31.1 ns), which are equivalent to the spectra. The contour map displayed in Fig. 8(c) exhibits the spectral-temporal evolution dynamics. The variation of the overall integrated energy within one round-trip time period is shown in Fig. 8(b). Analogous to the case displayed in Fig. 3, there exists turbulent oscillation in the initial stages of the pulse establishment, following a giant leap known as the *Q*-switched pulse [see the zoom-in figures in the right column of Fig. 8(c), panels (i) and (ii)]. However, the spectral turbulence only occurs during the formation of a single soliton, that is, the pulse on the top in Fig. 8(c). As for the other three pulses, they rise up later and do not behave the same way as the first-established soliton. The energy variation in Fig. 8(b) also exhibits substantial differences between the two channels, including in the turbulent process (see the inset from the 6500th round trip to the 6700th round trip). In contrast to the buildup dynamics shown in Fig. 3 in the main text, the giant spikes (i.e., the giant intensity fluctuations) do not appear after the generation of all four solitons. The corresponding

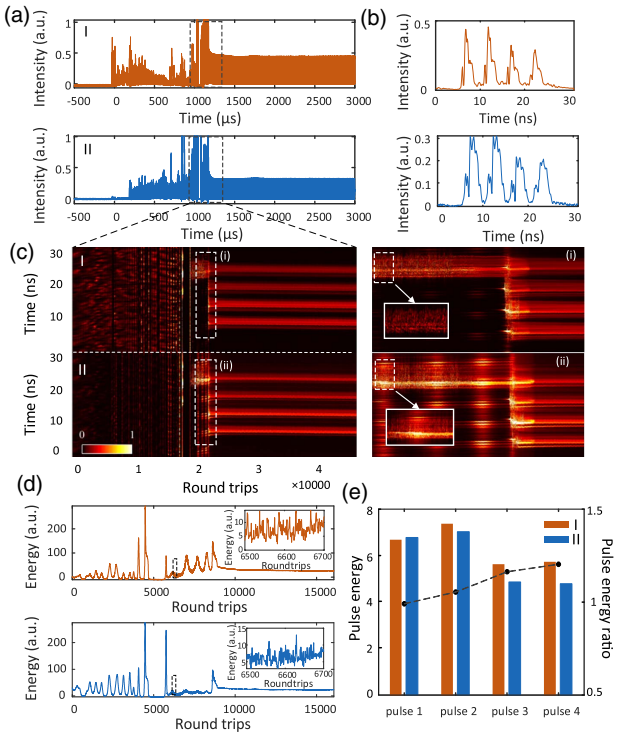

Fig. 8. Buildup dynamics of a four-soliton STML. (a) Real-time experimental data acquired from channel I (orange) and channel II (blue); (b) corresponding stretched pulse waveforms after stable STML within one cavity FSR (~31.1 ns); (c) overall energy variation during the buildup process. The selected data ranges are denoted by the black dashed rectangle in (a). The insets are the zoom-in waveforms showing the turbulent phase. (d) 2D contour plot of the four-soliton buildup process. The white dashed rectangles in (i) and (ii) refer to (c), the zoom-in figures exhibiting the establishment of the multiple-soliton in the right column. (e) Integrated pulse energy of channel I (orange) and channel II (blue). The ratios of pulse energy between two channels for each pulse are drawn with the black dashed line.

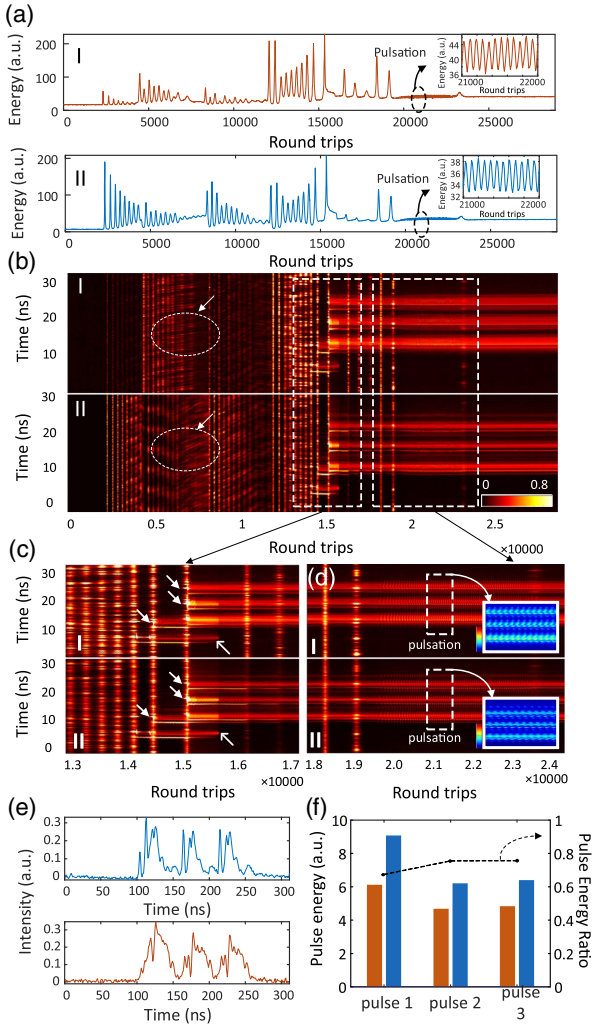

Fig. 9. Dynamics of the buildup of a three-soliton STML, including a pulsation process. (a) 2D contour plot showing the buildup dynamics of the three-soliton STML. The white circles highlight the pulse evolution distinction between the two channels during RO. (b) Zoom-in figures displaying the details near the soliton establishments. The white arrows denote the moments when the solitons rise up or annihilate. (c) Zoom figures of the pulsation process. The insets are the magnified figures showing the spectral evolution, extracted from a certain round-trip range denoted by the white rectangles. (d) Corresponding overall energy variation versus round trip. The insets are the zoom-in figures exhibiting the pulsation (breathing) behavior. (e) Stretched pulse profiles of channels I and II after steady mode locking; (f) integrated pulse energy. The dashed line represents the ratios of pulse energy between the two channels for each pulse.

buildup animation of this four-soliton STML is shown in Visualization 1.

Additionally, we integrate the spectral energy of each individual soliton in the two channels after stable mode locking, just as what we did in the case in Fig. 3. The results are shown in Fig. 8(d), with the pulse energy ratio denoted by the black dashed line. It can be inferred that solitons are generated with different mode components, which leads to the distinction of the energy ratios (over the two channels) among the pulses. This phenomenon also implies the spatiotemporal structures of the multiple solitons.

We show another buildup process of a three-pulse STML in Fig. 9, which contains a pulsation process after the establishment of the pulses. The corresponding 2D contour map is plotted in Fig. 9(a). Analogous to all the other multiple-soliton buildup cases, there exist substantial distinctions between the channels during RO and Q switching. For example, denoted by the black dashed circles in Fig. 9(a), the small pulse drifting speed is higher in channel II than in channel I, clearly shown in the evolving patterns. Figures 9(b) and 9(c) display, respectively, the zoom-in spectral evolution near the establishment of the pulses and the pulsation period. The white arrows in Fig. 9(b) denote the time point where the solitons rise up and annihilate. The soliton buildup moment varies from pulse to pulse in this case, specifically, all following giant energy fluctuations (i.e., the Q-switched pulse). As for the pulsation, the spectral evolution patterns belonging to different transverse modes have slight differences [see the zoom-in insets of Fig. 9(c)]. This phenomenon is coincident with the discoveries in Ref. [30]. The integrated overall energy versus round trip is displayed in Fig. 9(d). The insets are the corresponding close-up of the energy variation during pulsation (or breathing) from the 21,000th to 22,000th roundtrip, which are denoted by the dashed circles and arrows. There, the energy variations from the two channels are synchronized, indicating no modal energy transition between the modes during the pulsation process. The stretched-pulse profiles after steady mode locking are displayed in Fig. 9(e). Figure 9(f) exhibits the pulse energy in the two channels and their relative ratios. In this case, pulses 2 and 3 are identical, and the pulse energy ratio between the channels is also the same (around 0.75).

APPENDIX D: DETAILS OF THE THEORETICAL MODEL AND SIMULATING PARAMETERS

The detailed theoretical model schematic is depicted in Fig. 10, which is adapted from the iterative method that was proposed in Refs. [34,35] by taking the transverse-mode coupling (mode composition and decomposition) and mode-dependent SA into account. Here we focus on the impact of the 3D SA on forming the spatiotemporal structures of the pulses. Nonlinear interactions among the transverse modes, e.g., modal gain competition effects and nonlinear propagations, are neglected in this model for simplicity. We consider the case of a K-soliton mode locking containing M transverse modes.

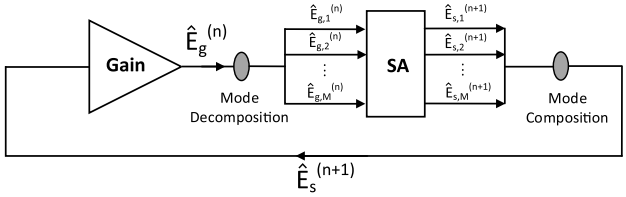

Fig. 10. Schematic of the numerical simulation model of multiple-soliton with multiple modes.

The energy of the pulses can be expressed as vectors $\hat{E}_g^{(n)}, \hat{E}_s^{(n)}$, which write

$$\hat{E}_g^{(n)} = [E_{g,P_1}^{(n)}, E_{g,P_2}^{(n)}, \cdots, E_{g,P_K}^{(n)}],$$
$$\hat{E}_s^{(n)} = [E_{s,P_1}^{(n)}, E_{s,P_2}^{(n)}, \cdots, E_{s,P_K}^{(n)}]. \quad \textbf{(D1)}$$

The superscript n stands for the number of iterations. $E_{g,P_1}^{(n)}, E_{g,P_2}^{(n)}, \cdots, E_{g,P_K}^{(n)}$ are the energy values of each individual pulse of the nth iteration from P_1 to P_K after the gain media, while $E_{s,P_1}^{(n)}, E_{s,P_2}^{(n)}, \cdots, E_{s,P_K}^{(n)}$ stand for the individual pulse energy after the SA, as denoted in Fig. 10. First, the transverse modes are amplified as a whole (i.e., there are no modal competitions) in the gain media while the multiple pulses still experience gain competition. The gain effects are described by the following equation:

$$E_{g,P_K}^{(n)} = \frac{g_{\text{net},0}}{1 + \left(\sum_{k=1}^{K} E_{s,P_K}^{(n)}\right)/E_{\text{sat}}}, \qquad k = 1, 2, \ldots, K, \quad \textbf{(D2)}$$

where E_{sat} represents the gain saturation energy and $g_{\text{net},0}$ denotes the small-signal net gain. Afterwards, the energies of the amplified pulses are linearly distributed to different modes according to the coupling ratio $\vec{x} = [x_1, x_2, \ldots, x_M]$ during mode decomposition, where M is the number of transverse modes. In this way, $\hat{E}_g^{(n)}$ is dissected into multiple vectors (i.e., a $K \times M$ matrix), which contains the pulse energy vectors belonging to different transverse modes. The decomposition can be expressed as

$$\hat{E}_{g,m}^{(n)} = x_m \hat{E}_g^{(n)}, \qquad m = 1, 2, \ldots, M, \quad \textbf{(D3)}$$

where $\hat{E}_{g,m}^{(n)} = [E_{g,P_1,m}^{(n)}, E_{g,P_2,m}^{(n)}, \ldots, E_{g,P_K,m}^{(n)}]$ represents the pulse energy vector of the mth mode. Then the mode-dependent SA effects are applied on the multimode pulses, which conform to

$$\hat{E}_{s,m}^{(n+1)} = \frac{1}{2}[1 - q_m \cos(\pi \hat{E}_{g,m}^{(n)} - \varphi_m)]\hat{E}_{g,m}^{(n)},$$
$$m = 1, 2, \ldots, M, \quad \textbf{(D4)}$$

wherein the parameters of the SA (i.e., the modulation depth q_m and the preset phase bias φ_m) could be diverse for different transverse modes, mainly a consequence of the intensity (thus space)-dependent SA effect [27]. The solitons are then mode-composited and return to the gain media, completing a cycle of the iterative model. Here $\hat{E}_{s,m}^{(n+1)} = [E_{s,P_1,m}^{(n+1)}, E_{s,P_2,m}^{(n+1)}, \ldots, E_{s,P_K,m}^{(n+1)}]$. The pulse energies of the mth mode after SA are denoted as $\hat{E}_{s,m}^{(n+1)}$. Finally, the pulses are linearly composited by another coupling ratio $\vec{y} = [y_1, y_2, \ldots, y_M]$, yielding

$$\hat{E}_s^{(n+1)} = \sum_{m=1}^{M} y_m \hat{E}_{s,m}^{(n+1)}, \quad \textbf{(D5)}$$

where the pulse energy vector $\hat{E}_s^{(n+1)}$ contains the energy value of the pulses in all modes and transmits back to the gain media, starting up the next iteration.

For the simulation cases exhibited in Fig. 4(b), the parameters are $g_{\mathrm{net},0} = 7.0, q = [q_1, q_2, q_3] = [0.585, 0.45, 0.36]$, $\varphi = [\varphi_1, \varphi_2, \varphi_3] = [-\pi/72, -\pi/24, -\pi/60]$, $x_1 = y_1 = 4/7$, $x_2 = y_2 = 2/7$, and $x_3 = y_3 = 1/7$. The energy values of the seed noises for the three pulses are 0.2, 0.18, 0.15 (i.e., $\hat{E}_s^{(0)} = [0.2, 0.18, 0.15]$). For each E_{sat}, the iteration is carried out for 500 cycles, which is adequate to ensure the iterative energy to reach stability.

Funding. National Natural Science Foundation of China (61905018, 61975090); Fundamental Research Funds for the Central Universities (2019XD-A09-3); State Key Laboratory of Information Photonics and Optical Communications (IPOC2019ZT04, IPOC2020ZT02); Beijing Nova Program of Science and Technology (Z191100001119110).

Acknowledgment. The authors thank Prof. Chengying Bao from Tsinghua University for helpful comments on this paper.

Disclosures. The authors declare no conflicts of interest.

Data Availability. Data underlying the results presented in this paper are not publicly available at this time but may be obtained from the authors upon reasonable request.

REFERENCES

1. P. Grelu and N. Akhmediev, "Dissipative solitons for mode-locked lasers," Nat. Photonics **6**, 84–92 (2012).
2. N. N. Akhmediev, A. Ankiewicz, and J. M. Soto-Crespo, "Multisoliton solutions of the complex Ginzburg-Landau equation," Phys. Rev. Lett. **79**, 4047–4051 (1997).
3. D. Y. Tang, L. M. Zhao, B. Zhao, and A. Q. Liu, "Mechanism of multisoliton formation and soliton energy quantization in passively mode-locked fiber lasers," Phys. Rev. A **72**, 043816 (2005).
4. B. G. Bale, K. Kieu, J. N. Kutz, and F. Wise, "Transition dynamics for multi-pulsing in mode-locked lasers," Opt. Express **17**, 23137–23146 (2009).
5. Y. Meng, S. Zhang, X. Li, H. Li, J. Du, and Y. Hao, "Multiple-soliton dynamic patterns in a graphene mode-locked fiber laser," Opt. Express **20**, 6685–6692 (2012).
6. A. Mahjoubfar, D. V. Churkin, S. Barland, N. Broderick, S. K. Turitsyn, and B. Jalali, "Time stretch and its applications," Nat. Photonics **11**, 341–351 (2017).
7. K. Goda and B. Jalali, "Dispersive Fourier transformation for fast continuous single-shot measurements," Nat. Photonics **7**, 102–112 (2013).
8. G. Herink, F. Kurtz, B. Jalali, D. R. Solli, and C. Ropers, "Real-time spectral interferometry probes the internal dynamics of femtosecond soliton molecules," Science **356**, 50–54 (2017).
9. K. Krupa, K. Nithyanandan, U. Andral, P. Tchofo-Dinda, and P. Grelu, "Real-time observation of internal motion within ultrafast dissipative optical soliton molecules," Phys. Rev. Lett. **118**, 243901 (2017).
10. Z. Q. Wang, K. Nithyanandan, A. Coillet, P. Tchofo-Dinda, and P. Grelu, "Optical soliton molecular complexes in a passively mode-locked fibre laser," Nat. Commun. **10**, 830 (2019).
11. X. Liu, X. Yao, and Y. Cui, "Real-time observation of the buildup of soliton molecules," Phys. Rev. Lett. **121**, 023905 (2018).
12. J. Peng and H. Zeng, "Build-up of dissipative optical soliton molecules via diverse soliton interactions," Laser Photon. Rev. **12**, 1800009 (2018).
13. P. Ryczkowski, M. Närhi, C. Billet, J. M. Merolla, G. Genty, and J. M. Dudley, "Real-time full-field characterization of transient dissipative soliton dynamics in a mode-locked laser," Nat. Photonics **12**, 221–227 (2018).
14. X. Wang, J. Peng, K. Huang, M. Yan, and H. Zeng, "Experimental study on buildup dynamics of a harmonic mode-locking soliton fiber laser," Opt. Express **27**, 28808–28815 (2019).
15. X. Liu and M. Pang, "Revealing the buildup dynamics of harmonic mode-locking states in ultrafast lasers," Laser Photon. Rev. **13**, 1800333 (2019).
16. Y. Yu, B. Li, X. Wei, Y. Xu, K. K. M. Tsia, and K. K. Y. Wong, "Spectral-temporal dynamics of multipulse mode-locking," Appl. Phys. Lett. **110**, 201107 (2017).
17. J. Zeng and M. Y. Sander, "Real-time transition dynamics between multi-pulsing states in a mode-locked fiber laser," Opt. Lett. **45**, 5–8 (2020).
18. L. G. Wright, D. N. Christodoulides, and F. W. Wise, "Spatiotemporal mode-locking in multimode fiber lasers," Science **358**, 94–97 (2017).
19. H. Qin, X. Xiao, P. Wang, and C. Yang, "Observation of soliton molecules in a spatiotemporal mode-locked multimode fiber laser," Opt. Lett. **43**, 1982–1985 (2018).
20. Y. Ding, X. Xiao, P. Wang, and C. Yang, "Multiple-soliton in spatiotemporal mode-locked multimode fiber lasers," Opt. Express **27**, 11435–11446 (2019).
21. T. Mayteevarunyoo, B. A. Malomed, and D. V. Skryabin, "Spatiotemporal dissipative solitons and vortices in a multi-transverse-mode fiber laser," Opt. Express **27**, 37364–37373 (2019).
22. H. Wu, W. Lin, Y. J. Tan, H. Cui, Z. C. Luo, W. C. Xu, and A. P. Luo, "Pulses with switchable wavelengths and hysteresis in an all-fiber spatio-temporal mode-locked laser," Appl. Phys. Express **13**, 022008 (2020).
23. U. Tegin, E. Kakkava, B. Rahmani, D. Psaltis, and C. Moser, "Spatiotemporal self-similar fiber laser," Optica **6**, 1412–1415 (2019).
24. T. Ugur, R. Babak, K. Eirini, P. Demetri, and M. Christophe, "Single-mode output by controlling the spatiotemporal nonlinearities in mode-locked femtosecond multimode fiber lasers," Adv. Photon. **2**, 056005 (2020).
25. K. Liu, X. Xiao, and C. Yang, "Observation of transition between multimode *Q*-switching and spatiotemporal mode locking," Photon. Res. **9**, 530–534 (2021).
26. X. Xiao, Y. Ding, S. Fan, C. Yang, and X. Zhang, "Period-doubling bifurcation in spatiotemporal mode-locked lasers," arXiv:2101.00149 (2020).
27. Y. Ding, X. Xiao, K. Liu, S. Fan, X. Zhang, and C. Yang, "Spatiotemporal mode-locking in lasers with large modal dispersion," Phys. Rev. Lett. **126**, 093901 (2021).
28. L. G. Wright, P. Sidorenko, H. Pourbeyram, Z. M. Ziegler, A. Isichenko, B. A. Malomed, C. R. Menyuk, D. N. Christodoulides, and F. W. Wise, "Mechanisms of spatiotemporal mode-locking," Nat. Phys. **16**, 565–570 (2020).
29. J. C. Jing, X. Wei, and L. V. Wang, "Spatio-temporal-spectral imaging of non-repeatable dissipative soliton dynamics," Nat. Commun. **11**, 2059 (2020).
30. Y. Guo, X. Wen, W. Lin, W. Wang, X. Wei, and Z. Yang, "Real-time multispeckle spectral-temporal measurement unveils the complexity of spatiotemporal solitons," Nat. Commun. **12**, 67 (2021).
31. A. B. Grudinin, D. J. Richardson, and D. N. Payne, "Energy quantisation in figure eight fibre laser," Electron. Lett. **28**, 67–68 (1992).
32. X. Liu, D. Popa, and N. Akhmediev, "Revealing the transition dynamics from *Q* switching to mode locking in a soliton laser," Phys. Rev. Lett. **123**, 093901 (2019).
33. L. M. Zhao, D. Y. Tang, H. Zhang, and X. Wu, "Bunch of restless vector solitons in a fiber laser with SESAM," Opt. Express **17**, 8103–8108 (2009).
34. F. Li, P. K. A. Wai, and J. N. Kutz, "Geometrical description of the onset of multi-pulsing in mode-locked laser cavities," J. Opt. Soc. Am. B **27**, 2068–2077 (2010).
35. L. Kong, X. Xiao, and C. Yang, "Operating regime analysis of a mode-locking fiber laser using a difference equation model," J. Opt. **13**, 105201 (2011).